

Simulations of Streamwise Vortices on a High-Lift Wing with UHBR-Engine

Tim Landa, Rolf Radespiel and Sebastian Ritter

Abstract Results of numerical simulations on a high-lift configuration with an Ultra High Bypass Ratio (UHBR) engine are shown. In the area of the integrated engine, a complex vortex-system develops. Different longitudinal vortices proceed downstream on the suction side influencing the local flowfield. Steady and unsteady numerical simulations are performed at different angles of attack. As flow solver the DLR TAU Code is used and the Menter-SST eddy viscosity turbulence model and the JHh-v2 Reynolds-Stress-Model are applied. The predicted vortex system is analyzed and the effect on the flow field and the local stall behavior is shown. In particular the effect of the turbulence models of different types on the prediction of the vortex system and the flowfield is presented.

1 Introduction

Airfoils of modern aircraft are designed to show good aerodynamic characteristics at cruise speed. However, creating enough lift at low-speeds during take-off and landing, high-lift systems are required. Common systems consist of slotted slats as leading edge device and slotted flaps as trailing edge device [20]. The fundamental effects of slotted high-lift devices increasing the maximum lift coefficient are well understood [22]. Nevertheless, at realistic configurations with integrated engine and finite high-lift devices complex flow features like longitudinal vortices occur. In general,

T. Landa (✉) · R. Radespiel
Institute of Fluid Mechanics, TU Braunschweig, Hermann-Blenk-Str. 37,
38108 Braunschweig, Germany
e-mail: t.landa@tu-braunschweig.de

R. Radespiel
e-mail: r.radespiel@tu-braunschweig.de

S. Ritter
Institute of Aerodynamics and Flow Technology, DLR Braunschweig,
Lilienthalplatz 7, 38108 Braunschweig, Germany
e-mail: sebastian.ritter@dlr.de

© Springer International Publishing AG 2018

A. Dillmann et al. (eds.), *New Results in Numerical and Experimental Fluid Mechanics XI*, Notes on Numerical Fluid Mechanics and Multidisciplinary Design 136, https://doi.org/10.1007/978-3-319-64519-3_4

the three-dimensional effects lead to a loss of maximum achievable lift [8] and have to be considered for maximum lift-prediction.

The complex flow of high-lift configurations at high angles of attack represent a challenging task for numerical flow simulation. Nevertheless, the increasing computational resources nowadays allow the simulation of complex three-dimensional configurations. In recent years, numerous projects addressed the flow prediction of high-lift configuration at maximum lift conditions. Within the European projects EUROLIFT and EUROLIFT II [18] high-lift configurations with different levels of complexity with and without engine have been investigated. The results show that the CFD methods are able to capture the influence of geometric details on the lift behavior. Nevertheless, Geyr et al. [7] show considerable differences between CFD and PIV concerning the prediction of a strake vortex. Within these simulations, the common Spalart-Allmaras (SA) eddy-viscosity model has been applied, underpredicting the vortex strength. Furthermore, discrepancies between numerical and experimental data concerning maximum lift occurred. Such differences for eddy-viscosity models concerning maximum lift prediction are also observed by Eliasson et al. [6]. In contrast, Reynolds Stress Models (RSM) show improved results. Within the research project HINVA (High Lift Inflight Validation) [19] detailed models of the A320 at high-lift conditions were investigated in numerical studies and compared with experimental data from inflight and wind-tunnel measurements. A major objective was to improve the accuracy of the prediction of the aerodynamic performance at high-lift conditions. Again, the results show, that the applied numerical methods are able to capture the important flow features for maximum lift. However, it turned out that accurate predictions at maximum lift conditions are still a challenging task [1]. Similar findings derive from simulations of the trap wing within the NASA High-Lift Prediction Workshop. Significant differences between simulations (Spalart-Allmaras and Menter-SST eddy-viscosity models) and experiments occur close to maximum lift [21]. Further simulations (SA, SST and RSM) on this configuration show that particularly the region close to the wing tip differs [5]. Here, the applied turbulence model has a large influence on the prediction of the wing tip vortex. Investigations of a wing tip vortex of a half-wing model without high-lift devices support this finding. Craft [4] and Cécora [3] showed a rapid decay of the vortex in simulations with eddy viscosity models. In contrast, Reynolds Stress Models are able to preserve the vortex downstream corresponding to experimental data. Since longitudinal vortices are important for stall aerodynamics, an accurate prediction of the vortices is required for precise maximum lift predictions. Hence, the application of RSM on complex high-lift configurations is a promising approach to improve the predictions at maximum lift conditions.

Recently, the authors presented results of simulations with the Menter-SST eddy viscosity model and the JHh-v2 RSM on a generic high-lift configuration without engine [10–12]. The vortex system emerging at the spanwise end faces of a finite slat and the corresponding step of the clean nose has been investigated. The results exhibit significant differences of the appearance and the interaction of the vortices depending on the applied turbulence model. Within the present contribution, the findings of the simulations on the generic configuration are transferred to a high-lift

configuration with an Ultra High Bypass Ratio (UHBR) engine. Ritter [17] recently performed a positioning study of the UHBR-engine on a similar configuration (with different sweep angle and flap settings). The experiences concerning the position of the engine are transferred without performing an additional positioning study on the present configuration.

2 Numerical Setup

2.1 Methods

For the simulations the DLR TAU Code is used as flow solver [13]. This software package solves the Reynolds-averaged Navier-Stokes equations (RANS) on structured, unstructured or hybrid grids based on a finite volume method. The TAU Code provides various convergence acceleration methods, like a multigrid approach and local time-stepping.

For the simulations presented within this contributions central flux discretization and implicit LU-SGS relaxation are applied. Steady simulations with local time-stepping and time-accurate simulations with a dual time-stepping approach are performed. All simulations use multigrids for convergence acceleration on three multigrid levels. For the determination of the Reynolds stresses within the RANS equation the Menter-SST model and the JHh-v2 RSM are applied. The Menter-SST (Shear Stress Transport) model is a two-equation eddy viscosity model following the hypothesis of Boussinesq to approximate the Reynolds stresses [14]. It is a robust and widely used turbulence model. However, the ability to accurately predict longitudinal vortices is known to be limited [3, 4]. In contrast, simulations with the JHh-v2 RSM show significant improvements in vortex prediction [3]. This model is based on the Jakirlić Hanjalić homogeneous (JHh) turbulence model [9]. Within this model, a transport equation for each component of the Reynolds stresses is solved. The model has been extended and implemented in the TAU Code by Probst and Radespiel [15] and recalibrated by Cécora [3] resulting in the JHh-v2 RSM version.

2.2 High-Lift Configuration

The high-lift configuration (illustrated in Fig. 1) is a backward swept wing based on the DLR F15 high-lift airfoil with periodic boundary conditions at each side of the computational domain. At 50% of the span, the UHBR-engine is integrated. At this position, the slat is intercepted due to the presence of the nacelle. The following parameters define the geometry:

- Span: $b = 34.736$ m
- Reference chord: $c_{ref} = 4.342$ m (chord of clean configuration)

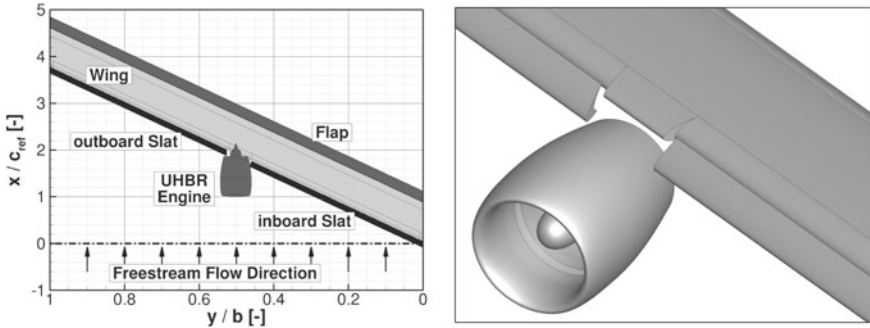


Fig. 1 High-lift configuration with UHBR-engine. *Left* top view on complete geometry, *right* close up 3D-view on engine and slat interception

- Sweep angle: $\varphi = 25^\circ$
- Reference area: $A = b \cdot c_{ref} = 150.824 \text{ m}^2$ (reference for C_L/C_D)
- Slat: 28.8° deflection, 2.09% overlap, 2.61% gap
- Flap: 30.3° deflection, 1.52% overlap, 0.968% gap
- UHBR-engine: $L = 4.95 \text{ m}$, $D_{a,max} = 2.92 \text{ m}$, Bypass Ratio = 17.1.

2.3 Grid

The computational grid has been created using the commercial software Gridgen (V 15.18, Pointwise, Inc.). It is a hybrid grid with structured parts (hexahedral cells and prisms) in the near-wall region and in the area downstream of the engine in the region of the vortex system. Detailed studies on the grid topology have been performed on a generic high-lift configuration [10–12]. The resulting grid topology is transferred to the configuration with UHBR-engine. To account for the increased Reynolds number, the distribution of grid points in the structured parts is adapted resulting in y^+ -values of approximately 1 largely. The computational domain is a swept cylinder with the length equal to the configurations span ($b = 34.736 \text{ m}$). The side faces of the domain are assumed as periodic planes. The cylinder radius equals $150 \cdot c_{ref}$ and the outer barrel surface represents the farfield boundary. In total, the grid consist of about 100 million points.

2.4 Flow Conditions

The model size and the flow conditions for the simulations correspond to typical landing conditions. Fluid properties are taken out of the International Standard

Atmosphere at ground level. Simulations at different angles of attack have been performed with the following conditions.

- $Re = 15.687 \times 10^6$ (corresponding to $c_{ref} = 4.342$ m)
- $Ma = 0.1655$
- $U_\infty = 57.76 \frac{m}{s}$
- $\alpha = 6^\circ/10^\circ/14^\circ$

The flow through the engine was defined with a fixed massflow at an inflow plane at the position of the fan. Two exhaust planes exist for the core flow and the flow that bypasses the core. At this planes pressure ratio and temperature ratio are specified. For all simulations with the Menter-SST model, turbulent flow is assumed. However, the JHh-v2 model requires transition positions to develop turbulence within the boundary layer (see also [16]). Corresponding to common practice, the transition positions for the JHh-v2 RSM are defined close to the suction peaks on the upper surface of each element [2]. On the lower surfaces, transition was set closely downstream of the stagnation line. Steady simulations have been performed at all incidences with the Menter-SST model and at $\alpha = 6^\circ$ with the JHh-v2 RSM. Since no satisfying results with the steady solver were achieved for higher incidences, time-accurate (unsteady) simulations have been performed at $\alpha = 10^\circ$ and $\alpha = 14^\circ$. For these simulations, the numerical solution was first initiated using a steady solver (local time stepping). Then, the time increment was chosen with $\Delta t = 1/1000 \cdot t_{conv} = 1/1000 \cdot c_{ref}/U_\infty$ and the flowfield was averaged over 500 timesteps ($\hat{=} 0.5 \cdot t_{conv}$).

3 Results

3.1 Convergence Behavior and Aerodynamic Coefficients

The steady simulations were performed until a constant behavior of the aerodynamic coefficient has been observed. The normalized density residual levels off in a range between 10^{-4} and 10^{-3} . The aerodynamic coefficients exhibit a periodically oscillating behavior. However, the fluctuations are limited and rather small. For this reason, the results with the steady solver are used for evaluation. Nevertheless, the simulations with the JHh-v2 RSM at $\alpha = 10^\circ$ and $\alpha = 14^\circ$ show significant non-regular fluctuations with the steady solver. Hence, unsteady simulations were performed for this cases. However, it has to be mentioned, that a rather short period of time ($0.5 \cdot t_{conv}$) is evaluated for these simulations and still irregular changes within the coefficients are observed. Due to limited resources of time and computational power, a longer period of time was not taken into account. The results for the aerodynamic coefficients are presented in Fig. 2 showing the mean values and the minimum and maximum deviations within the considered period.

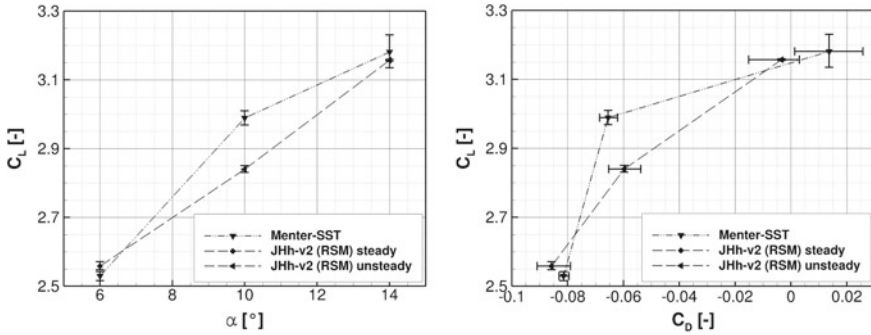


Fig. 2 Aerodynamic coefficients predicted with Menter-SST and JHh-v2 turbulence models. *Left* lift versus angle of attack (lift curve), *right* lift versus drag (Lilienthal polar)

Significant differences between both turbulence models occur at $\alpha = 10^\circ$. The results show increased suction peaks over the whole span with the Menter-SST model (not shown here) resulting in an increased lift coefficient for this incidence. Furthermore, the unsteady JHh-v2 simulation shows rather large changes in the lift coefficient. We note that the unconverged steady restart solution could have an influence on the unsteady flowfield. A leveled unsteady simulations over a larger period of time would be necessary to check, if the lift coefficient further increases with time.

3.2 Streamwise Vortices and Stall Mechanism

The computations reveal a system of different vortices close to the integrated engine. The appearance of the vortices and the effect on the flow field strongly depends on the angle of attack. Figure 3 shows streamtraces and regions of separated flow on the surface predicted with both turbulence models.

At $\alpha = 6^\circ$ footprints of different vortices occur downstream of the side faces of the slats and the clean nose. Furthermore, the JHh-v2 RSM predicts a small region of separated flow on the clean nose behind the engine. In contrast, the Menter-SST model predicts attached flow here. At $\alpha = 10^\circ$ both turbulence models predict a local limited area of separated flow on the clean nose. The size of the area is slightly increased compared to $\alpha = 6^\circ$. In addition, another region of separated flow develops downstream of the inboard edge of the clean nose. At $\alpha = 14^\circ$ the separation extends over the whole depth of the main wing on nearly the whole clean nose part. Only a small region outboard still shows attached flow. Furthermore, the JHh-v2 RSM predicts an onset of separation starting from the edge of the inboard slat. In contrast, the steady Menter-SST simulation only predicts a rather small spot of separation at this position. The differences between the predictions of both turbulence models result from the vortices, which strongly influence the flow in this region. Figure 4

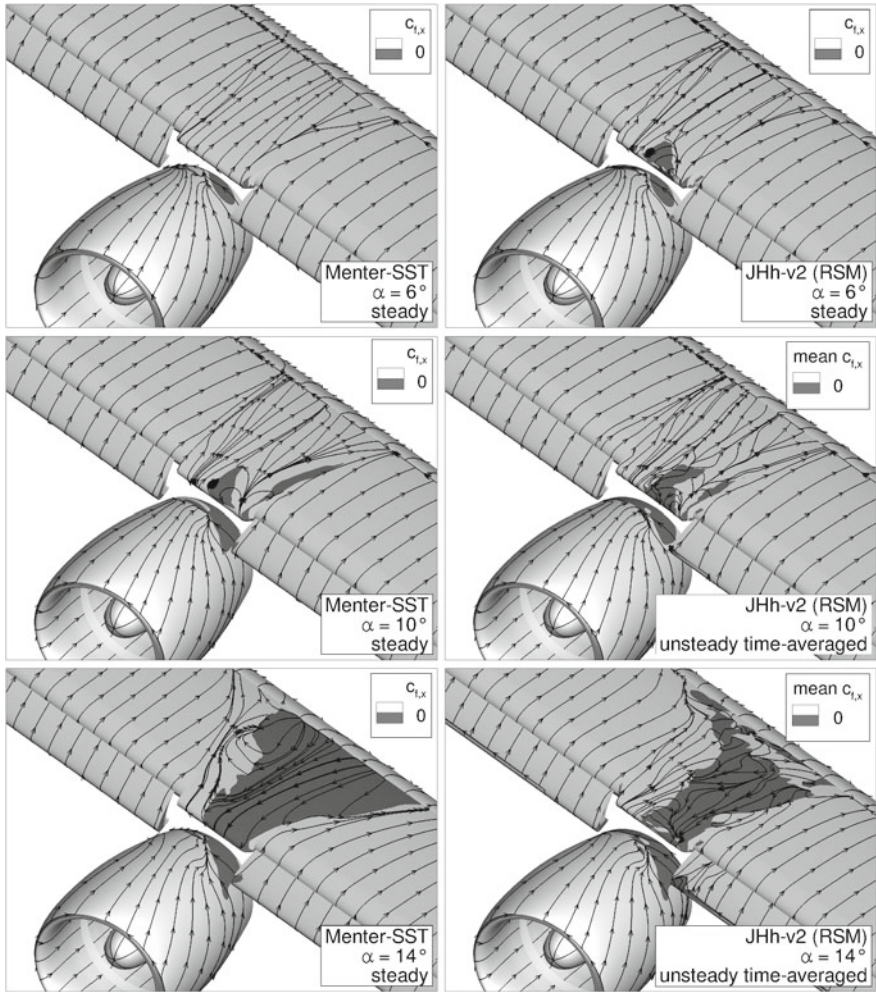


Fig. 3 Streamtraces and regions of separated flow. *Left* Menter-SST (steady), *right* JHh-v2 RSM ($\alpha = 6^\circ$ steady, $\alpha = 10^\circ/14^\circ$ unsteady time-averaged)

shows a visualization of the vortices predicted with both turbulence models using the normalized Q-criterion.

Significant differences in the prediction of the vortices occur between both models. In general, the JHh-v2 RSM provides stronger vortices, which are preserved while proceeding downstream. In contrast, the vortices dissipate faster within the Menter-SST simulations. At $\alpha = 6^\circ$ the JHh-v2 RSM shows a distinct vortex developing above the nacelle trailing downstream above the clean nose. This vortex appears weaker in case of the Menter-SST model at this incidence resulting in the different effects on the surface at this angle of attack discussed above. At $\alpha = 10^\circ$

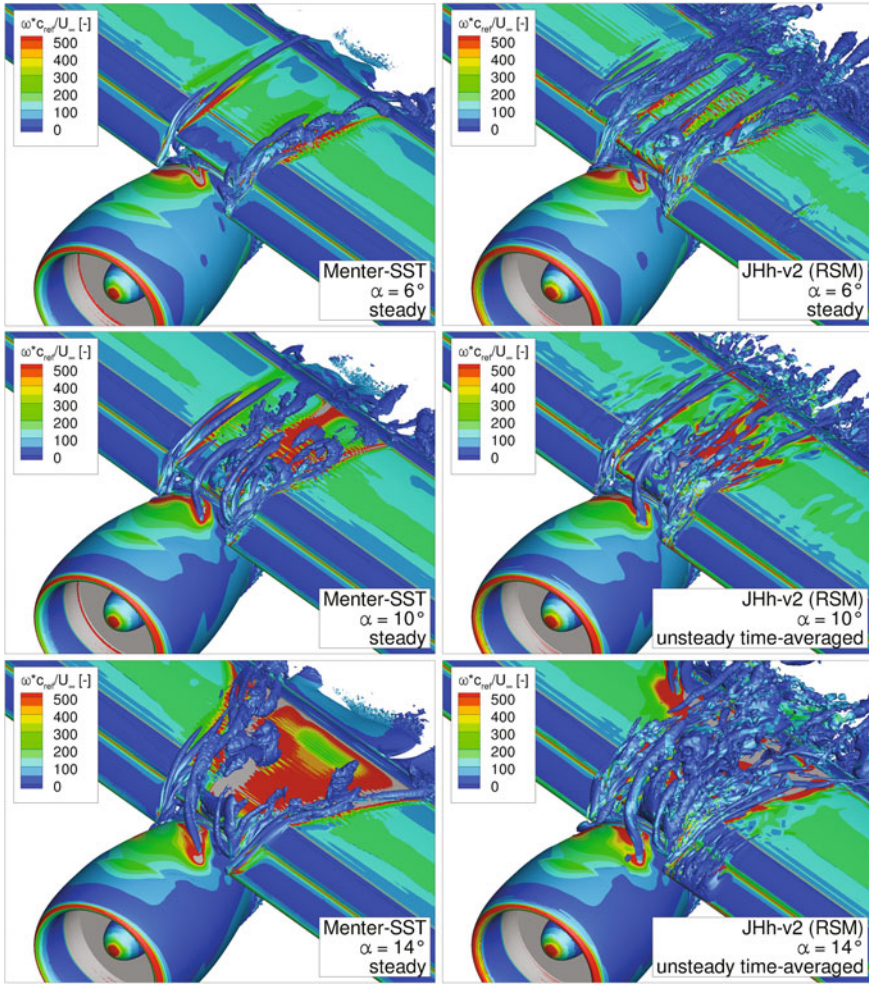


Fig. 4 Visualization of vortices. Iso-Surfaces of non-dimensional Q-criterion ($Q * (c_{ref})^2 / (U_\infty)^2 = 60$) colored with non-dimensional vorticity ($\omega * c_{ref} / U_\infty$). *Left* Menter-SST (steady), *right* JHh-v2 RSM ($\alpha = 6^\circ$ steady, $\alpha = 10^\circ/14^\circ$ unsteady time-averaged)

the vortices are pronounced more clearly with the Menter-SST model. The structures close to the leading edge are predicted similar as with the JHh-v2 RSM. Hence, the differences on the surface are rather small between the two models. Nevertheless, the JHh-v2 model again preserves the vortices longer. Similar findings hold for $\alpha = 14^\circ$. Furthermore, at this incidence vortical structures occur on the inboard slat close to the edge corresponding to the beginning separation shown above. The different prediction of the vortex system also influences the spanwise distribution of the lift coefficient shown in Fig. 5.

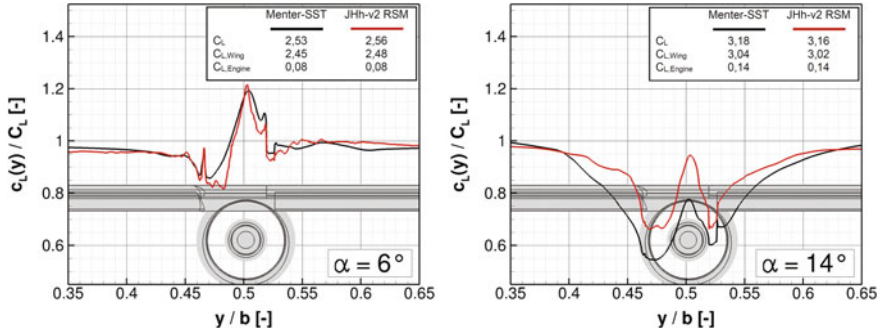


Fig. 5 Spanwise lift-distribution of the wing (lift of engine excluded) in the area of the integrated engine at $\alpha = 6^\circ$ (left) and $\alpha = 14^\circ$ (right)

At $\alpha = 6^\circ$ both models predict a similar behavior. Losses of the lift coefficient occur at the positions, where the slats end. Furthermore, the JHh-v2 RSM exhibits a decreased lift coefficient at the inboard part of the clean nose, corresponding to the position of the local separation shown in Fig. 3. At the outboard part of the clean nose, both models show an increased lift coefficient. At $\alpha = 14^\circ$ the large separation on the wing behind the engine causes a significant drop of the local lift coefficient. However, the Menter-SST model predicts stronger losses compared to the JHh-v2 RSM. Again, the lowest values of the local lift coefficient occur close to the edges of the slats and the clean nose and at the inboard part of the clean nose.

4 Conclusion

Results of numerical simulations with the Menter-SST model and the JHh-v2 RSM on a high-lift configuration with an Ultra High Bypass Ratio engine have been presented. The numerical settings and the computational grid have been successfully adapted from a generic configuration analyzed recently [10–12]. In particular, the vortex system of the integrated engine and the effect on the local stall behavior has been investigated. Local stall is observed on the inboard part of the clean nose behind the engine. In general, the overall stall behavior is predicted similar with both turbulence models. Nevertheless, differences concerning areas of separated flows are observed between the models. It has been shown, that particularly the prediction of the vortices in this region differs. The JHh-v2 RSM shows vortices, which are more pronounced. In addition, the vortices are preserved longer while proceeding downstream.

Unfortunately, no experimental data for both configurations with and without engine are available at present. Hence, a statement about the accuracy of the predicted vortices is not possible at the moment. Currently, a Detached Eddy Simulation is performed on the generic high-lift configuration. The results will show, if a

scale-resolving simulation will provide a different prediction of the vortices. Further conclusions concerning the influence of the turbulence modelling on the prediction of the vortices will be possible.

Acknowledgements The authors wish to acknowledge the German Federal Ministry for Economic Affairs and Energy (BMWi) for funding this research activity (grant number: 20A1301B). The views and conclusions contained herein are those of the authors and should not be interpreted as necessarily representing the official policies or endorsements, either expressed or implied, of the BMWi or the German government. Furthermore, the authors would like to thank the North-German Supercomputing Alliance (HLRN) for providing computational resources within the project nii00091.

Gefördert durch:



aufgrund eines Beschlusses
des Deutschen Bundestages

References

1. Bier, N., Rohlmann, D., Rudnik, R.: Numerical Maximum Lift Prediction of a Realistic Commercial Aircraft in Landing Configuration. AIAA 2012-0279, Nashville (2012)
2. Cécora, R.-D., Probst, A., Radespiel, R.: Advanced Reynolds stress turbulence modeling of subsonic and transonic flows. In: Second Symposium “Simulation of Wing and Nacelle Stall”, June 22nd–23rd, Braunschweig (2010)
3. Cécora, R.-D., Radespiel, R., Eisfeld, B., Probst, A.: Differential Reynolds-Stress modeling for aeronautics. *J. Aircr.* **53**(3), 739–755 (2015)
4. Craft, T.J., Gerasimov, A.V., Launder, B.E., Robinson, C.M.E.: A computational study of the near-field generation and decay of wingtip vortices. *Int. J. Heat Fluid Flow* **27**, 684–695 (2006)
5. Crippa, S., Melber-Wilkending, S., Rudnik, R.: DLR Contribution to the First High Lift Prediction Workshop. AIAA 2011-938, Orlando (2011)
6. Eliasson, P., Catalano, P., Le Pape, M.-C., Ortmann, J., Pelizzari, E., Ponsin, J.: Improved CFD Predictions for High Lift Flows in the European Project EUROLIFT II. AIAA 2007-4303, Miami (2007)
7. Frhr. v. Geyr, H., Schade, N., v. d. Burg, J.W., Eliasson, P., Esquieu, S.: CFD Prediction of Maximum Lift Effects on Realistic High-Lift-Commercial-Aircraft-Configurations Within the European Project EUROLIFT II. AIAA 2007-4299, Miami (2007)
8. Haines, A.B., Young, A.D.: Scale effects on aircraft and weapon aerodynamic. *AGARDograph* **323**, 27–65 (1994)
9. Jakirlic, S., Hanjalic, K.: A new approach to modelling near-wall turbulence energy and stress dissipation. *J. Fluid Mech.* **459**, 139–166 (2002)
10. Landa, T., Wild, J., Radespiel, R.: Simulation of longitudinal vortices on a high-lift wing. In: Radespiel, R., et al. (eds.) *Advances in Simulation of Wing and Nacelle Stall. Notes on Numerical Fluid Mechanics and Multidisciplinary Design*, vol. 131, pp. 351–366. Springer. ISBN 978-3-319-21126-8 (2016)
11. Landa, T., Radespiel, R., Wild, J.: Numerical Simulations of Streamwise Vortices on a Generic High-Lift Configuration. AIAA 2016-0304, San Diego (2016)
12. Landa, T., Wild, J., Radespiel, R.: Numerical simulations of streamwise vortices on a high-lift wing. *CEAS Aeronaut. J.* (2016). <https://doi.org/10.1007/s13272-016-0217-0>

13. Langer, S., Schwöppe, A., Kroll, N.: The DLR Flow Solver TAU—Status and Recent Algorithmic Developments. AIAA 2014-0080, National Harbor (2014)
14. Menter, F.R.: Zonal Two Equation $k-\omega$ Turbulence Models for Aerodynamic Flows. AIAA 93-2906, Orlando (1993)
15. Probst, A., Radespiel, R.: Implementation and Extension of a Near-Wall Reynolds-Stress Model for Application to Aerodynamic Flows on Unstructured Meshes. AIAA 2008-770, Reno (2008)
16. Probst, A., Radespiel, R., Rist, U.: Linear-stability-based transition modeling for aerodynamic flow simulations with a near-wall Reynolds-Stress model. AIAA J. **50**(2), 416–428 (2012)
17. Ritter, S.: Impact of different UHBR-Engine positions on the aerodynamics of a high-lift-wing. In: Radespiel, R., et al. (eds.) Advances in Simulation of Wing and Nacelle Stall. Notes on Numerical Fluid Mechanics and Multidisciplinary Design, vol. 131, pp. 367–380. Springer. ISBN 978-3-319-21126-8 (2016)
18. Rudnik, R., Frhr. v. Geyr, H.: The European High Lift Project EUROLIFT II—Objectives, Approach, and Structure. AIAA 2007-4296, Miami (2007)
19. Rudnik, R., Reckzeh, D., Quest, J.: HINVA—High Lift INflight Validation—Project Overview and Status. AIAA 2012-0106, Nashville (2012)
20. Rudolph, P.K.C.: High-Lift Systems on Commercial Subsonic Airliners. NASA CR 4746 (1996)
21. Sclafani, A.J., Slotnick, J.P., Vassberg, J.C., Pulliam, T.H., Lee, H.C.: Overflow Analysis of the NASA Trap Wing Model from the First High Lift Prediction Workshop. AIAA 2011-866, Orlando (2011)
22. Smith, A.M.O.: High lift aerodynamics. J. Aircr. **12**(6), 501–530 (1975)